AIAA JOURNAL
Vol. 42, No. 3, March 2004

Large-Eddy Simulation of High-Reynolds-Number Wall-Bounded Flows

C. Fureby,* N. Alin,† and N. Wikström†
Swedish Defence Research Agency, SE-172 90 Stockholm, Sweden
S. Menon‡
Georgia Institute of Technology, Atlanta, Georgia 30332-0150
N. Svanstedt§
Chalmers University of Technology, SE-412 96 Göteborg, Sweden
and
L. Persson¶
Swedish Defence Research Agency, SE-901 82 Umeå, Sweden

Large-eddy simulation (LES) of wall-bounded flows becomes prohibitively expensive at high Reynolds numbers if one attempts to resolve the small but dynamically important vortical structures in the near-wall region. The LES wall-boundary condition problem is thus to account for the effects of the near-wall turbulence between the wall and the first node and its transfer of momentum to the wall. Here we state the problem and give a brief overview of methods currently in use and possible future methods. To illustrate the problem and quantify the accuracy of some of the models, we present a few results from test cases ranging from fully developed turbulent channel flows to three-dimensional problems of practical engineering interest.

I. Introduction

ALMOST all practical flows are turbulent, and hence the simulation of turbulent flow remains one of the most challenging areas in the field of classical physics. Most computational-fluid-dynamic (CFD) codes presently used for high-Reynolds (Re)-number complex flows are based on Reynolds-averaged Navier–Stokes (RANS) equations[1–3] together with a turbulence model, for example, Ref. 2, for representing the effects of turbulence on the mean flow. Although RANS correctly predicts the mean flow in many cases, it often fails when facing more complex flows. Moreover, RANS is not appropriate when unsteady flow features dominate the flow. On the other hand, direct numerical simulation (DNS), in which all flow scales are properly resolved, is currently considered too expensive for most practical engineering flow problems.

Large-eddy simulations (LES)[3–8] present an alternative way of improving qualitative and quantitative aspects of complex turbulent flow predictions for both research and engineering purposes. LES resolves the three-dimensional time-dependent details of the large and medium (i.e., resolved) scales, whereas the effects of the small unresolved eddies are modeled with a subgrid turbulence model. The separation into grid and subgrid scales is often accomplished by a low-pass filter tied to the grid, but other methods are now also slowly coming into use (see Ref. 9 and references therein). After three decades of intensive research, and despite some yet unresolved issues, LES is currently considered the most promising method for studying complex flows. Although it will remain expensive in terms of CPU time and memory, LES presents the only reliable and practical method for simulating complex flows where RANS is inadequate.

Wall-bounded flows are characterized by much less universal properties than free flows and are thus more challenging to compute. Within the viscous sublayer, the characteristic length is set by the friction velocity u_τ and the viscosity ν, and outside of this the distance from the wall provides the appropriate scaling. As Reynolds number increases and the thickness of the viscous sublayer decreases, the number of grid points required to resolve the near-wall flow structures increases. Bagget et al.[10] estimated that the number of grid points required for a wall-resolved LES scales as $\mathcal{O}(Re_\tau^2)$, where Re_τ is the friction velocity-based Reynolds number. Moreover, unless the grid is sufficiently fine the anisotropy of the flow will cause anisotropy of the subgrid flow, necessitating subgrid models capable of handling simultaneous flow and grid anisotropy. Consequently, high-Reynolds-number flows, especially in complex geometries, are too expensive to compute with LES unless particular techniques are invoked to alleviate the severe resolution requirements near the wall. In principle this can be achieved by following either of the approaches listed here: 1) modify a traditional subgrid model to accommodate integration all the way to the wall; 2) use separate wall models; and 3) use subgrid simulation models, which can be based on multiscale methods.

The aim of this paper is twofold: 1) to summarize and compare LES models (i.e., the subgrid model with or without wall treatment) with DNS and experimental data for canonical boundary layer flows and 2) to apply selected models to flows around moderately complex geometries at high Reynolds number in order to investigate the capabilities and limitations of current LES. The second, third, and fourth sections deal with conventional, alternative, and emerging LES methods, respectively. In Sec. V the numerical methods used are briefly presented, whereas Secs. VI, VII, and VIII deal with fully developed turbulent channels flows, flow around a three-dimensional surface-mounted hill, and the flow around an inclined prolate spheroid, respectively. These two latter cases represent "real" flows, which are simulated with resolutions that are practical so that these results are reality checks on practical use of

Presented as Paper 2003-0066 at the AIAA 41st Aerospace Sciences Meeting, Reno, NV, 6–9 January 2003; received 20 July 2003; revision received 8 October 2003; accepted for publication 23 October 2003. Copyright © 2003 by the American Institute of Aeronautics and Astronautics, Inc. All rights reserved. Copies of this paper may be made for personal or internal use, on condition that the copier pay the $10.00 per-copy fee to the Copyright Clearance Center, Inc., 222 Rosewood Drive, Danvers, MA 01923; include the code 0001-1452/04 $10.00 in correspondence with the CCC.

*Director of Research, FOI, Department of Weapons and Protection, Warheads and Propulsion.
†Researcher, Department of Weapons and Protection, Warheads and Propulsion.
‡Professor, School of Aerospace Engineering.
§Professor, Department of Mathematics.
¶Researcher, FOI, Department of NBC Defence Environment and Protection.

LES. In Sec. IX we summarize our findings and put them in a wider perspective.

II. Conventional LES

In LES the flow variables are decomposed into large-scale components (denoted by overbars) and small-scale (subgrid) components (denoted by primes) by applying a filtering operation,

$$\bar{f}(\boldsymbol{x},t) = G * f(\boldsymbol{x},t) = \int_D G(\boldsymbol{x}-\boldsymbol{z},\Delta) f(\boldsymbol{z},t) d^3\boldsymbol{z} \qquad (1)$$

where G is the filter and Δ the filter width. Applying the filtering operation to the Navier–Stokes equations (NSE) yields

$$\nabla \cdot \bar{\boldsymbol{v}} = -m^{\rho}$$

$$\partial_t(\bar{\boldsymbol{v}}) + \nabla\cdot(\bar{\boldsymbol{v}}\otimes\bar{\boldsymbol{v}}) = -\nabla\bar{p} + \nabla\cdot\bar{\boldsymbol{S}} - \nabla\cdot\boldsymbol{B} - \boldsymbol{m}^{v} \qquad (2)$$

where $\bar{\boldsymbol{v}}$ is the velocity, $\bar{p}$ the pressure, $\bar{\boldsymbol{S}} = 2\nu\bar{\boldsymbol{D}}$ the viscous stress tensor, $\bar{\boldsymbol{D}} = \frac{1}{2}(\nabla\bar{\boldsymbol{v}} + \nabla\bar{\boldsymbol{v}}^T)$ the rate-of-strain tensor, and ν the viscosity. Specific to the LES model (2) are the subgrid-stress tensor $\boldsymbol{B} = \overline{\boldsymbol{v}\otimes\boldsymbol{v}} - \bar{\boldsymbol{v}}\otimes\bar{\boldsymbol{v}}$ and the commutation errors terms $m^{\rho} = [G*,\nabla]\boldsymbol{v}$ and $\boldsymbol{m}^{v} = [G*,\nabla](\boldsymbol{v}\otimes\boldsymbol{v} + p\boldsymbol{I} - \boldsymbol{S})$, where $[G*,\nabla]f = \overline{\nabla f} - \nabla\bar{f}$ is the commutation operator.[11,12] Only the resolved scales are thus retained in LES, whereas the subgrid-scale flow physics is grouped into $\boldsymbol{B}$, which has to be modeled using a functional expression of the type $\boldsymbol{B}(\boldsymbol{x},t) = \boldsymbol{B}[\bar{\boldsymbol{v}}(\boldsymbol{x}',t');\boldsymbol{x},t]$. Physical arguments and mathematical analysis, for example, Refs. 12–14, suggest that 1) $\boldsymbol{B}$ is invariant under a change of frame; 2) $\boldsymbol{B}$ is positive-definite symmetric, provided that $G = G(\boldsymbol{x},\Delta)$ is symmetric; and 3) that the inequalities $k = \frac{1}{2}\mathrm{tr}\boldsymbol{B} \geq 0$, $k^2 \geq \|\boldsymbol{B}\|^2$, and $\det\boldsymbol{B} \geq 0$ must be satisfied for $\boldsymbol{B}$ to be positive definite. Moreover, using Taylor-series expansion techniques it can be shown (e.g., Carati et al.[15] that $\boldsymbol{B}$ can be expanded as

$$\boldsymbol{B} = \overline{\boldsymbol{v}\otimes\boldsymbol{v}} - \bar{\boldsymbol{v}}\otimes\bar{\boldsymbol{v}} = \sum_{p,q=0,\infty;(p,q)\neq(0,0)} C_{\mathrm{pq}}(G)(\nabla_p\bar{\boldsymbol{v}})(\nabla_q\bar{\boldsymbol{v}}) \qquad (3)$$

where $\nabla_p = \partial^p/\partial x^p$ and $C_{\mathrm{pq}}(G)$ defines a sequence of grid moment-of-inertia tensors that depend on the filter kernel G and the filter width. Because of the symmetry of G, this expansion has only even-order terms, and hence the exact form of $\boldsymbol{B}$ is determined by G through C_{pq}. The commutation error terms (m^{ρ} and $\boldsymbol{m}^{v}$) reflect the fact that filtering and differentiation do not generally commute, for example, Refs. 13 and 16, the effects of which are not yet fully understood.

A. Subgrid-Scale Modeling

Two principal modeling strategies for $\boldsymbol{B}$ exist. Functional modeling consists of modeling the action of the subgrid scales on the resolved scales. This is basically of an energetic nature so that the balance of the energy transfer between the resolved and unresolved scale ranges is sufficient to describe the subgrid effects.[6] The energy cascade mechanism can thus be represented by

$$\boldsymbol{B}_D \approx \boldsymbol{B} - \tfrac{2}{3}k\boldsymbol{I} = -2\nu_k\bar{\boldsymbol{D}}, \qquad k = \tfrac{1}{2}\mathrm{tr}\boldsymbol{B} \qquad (4)$$

where ν_k is the subgrid eddy viscosity. To close Eq. (4), we need models for ν_k and k, and to this end we presume scale separation between the grid and subgrid scales. Among these models we have the one-equation eddy-viscosity model (OEEVM)[17]

$$\partial_t(k) + \nabla\cdot(k\boldsymbol{v}) = 2\nu_k\|\bar{\boldsymbol{D}}\|^2 + \nabla\cdot[(\nu+\nu_k)\nabla k] + c_\varepsilon k^{\frac{3}{2}}/\Delta$$

$$\nu_k = c_k\Delta k^{\frac{1}{2}} \qquad (5)$$

and the Smagorinsky (SMG) model[18]

$$k = c_I\Delta^2\|\bar{\boldsymbol{D}}\|^2, \qquad \nu_k = c_D\Delta^2\|\bar{\boldsymbol{D}}\| \qquad (6)$$

where the model coefficients (c_I, c_D, c_k, and c_ε) are evaluated either from a $|\boldsymbol{k}|^{-5/3}$ inertial subrange behavior, resulting in constant coefficients or from a dynamic procedure, producing spatio-temporally varying coefficients being functions of the resolved flowfield. Different dynamic procedures have been suggested, such as the dynamic Smagorinsky model (DSMG),[19] the one-equation dynamic localization model[20] the Lagrangian dynamic model,[21] and the localized dynamic kinetic energy model (LDKM).[22,23] These models all suffer from the assumption that $\boldsymbol{B} \propto \bar{\boldsymbol{D}}$, that is, that the eigenvectors of $\boldsymbol{B}$ are parallel to those of $\bar{\boldsymbol{D}}$, which is usually not the case in filtered DNS data, and they do not comply with Eq. (3).

Structural modeling consists of modeling $\boldsymbol{B}$ without incorporating any knowledge of the detailed nature of the interactions between the resolved and unresolved scales, for example, Ref. 6. Structural models are theoretically superior to functional models because they do not rely on isotropy on which most functional models are based. Among the best examples of structural models are the scale-similarity model (SSM) and mixed model (MM) of Bardina et al.,[24]

$$\boldsymbol{B} = \overline{\bar{\boldsymbol{v}}\otimes\bar{\boldsymbol{v}}} - \bar{\bar{\boldsymbol{v}}}\otimes\bar{\bar{\boldsymbol{v}}} - 2\nu_k\bar{\boldsymbol{D}} \qquad (7)$$

and the differential stress equation model (DSM) of Deardorff, for example, Refs. 25 and 26. The DSM uses a modeled transport equation for the subgrid-stress tensor $\boldsymbol{B}$ of the form

$$\partial_t(\boldsymbol{B}) + \nabla\cdot(\boldsymbol{B}\otimes\bar{\boldsymbol{v}}) = -(\bar{\boldsymbol{L}}\boldsymbol{B}^T + \boldsymbol{B}\bar{\boldsymbol{L}}^T) + \nabla\cdot(\nu_k\nabla\boldsymbol{B})$$

$$- c_m\left(k^{\frac{1}{2}}/\Delta\right)\boldsymbol{B}_D + \tfrac{2}{5}k\bar{\boldsymbol{D}}_D + \left(\tfrac{2}{3}c_m - c_\varepsilon\right)\left(k^{\frac{3}{2}}/\Delta\right)\boldsymbol{I} \qquad (8)$$

with $\nu_k = c_k\Delta k^{1/2}$ and $k = \frac{1}{2}\mathrm{tr}\boldsymbol{B}$. In Eq. (8) the terms on the right-hand side represent production, diffusion, return to isotropy, and mean strain of the pressure velocity gradient and dissipation, respectively. The model coefficients are evaluated from a $|\boldsymbol{k}|^{-5/3}$ inertial subrange behavior and take the values $c_m = 4.13$, $c_k = 0.07$, and $c_\varepsilon = 1.35$ respectively. Other models of this category include the nonlinear anisotropic models of Lund and Novikov.[27] The advantage of structural models over functional models is that the eigenvectors of $\boldsymbol{B}$ and $\bar{\boldsymbol{D}}$ are not parallel to each other, whereas a disadvantage might be the lack of dissipation. Moreover, the SSM and MM comply with Eq. (3).

B. Near-Wall Flow Physics and Modeling

LES of wall-bounded flows becomes prohibitively expensive at high Reynolds numbers if one attempts to resolve the small but dynamically important eddies in the near-wall region. These structures can be captured in a wall-resolved LES in which the grid is approximatively such that $\Delta x^+ < 200$, $\Delta y^+ < 2$, and $\Delta z^+ < 30$. Here, $+$ denotes nondimensionalization by the viscous length scale ν/u_τ and the friction velocity $u_\tau = \tau_w^{1/2}$, where $\tau_w = \nu(\partial v/\partial y)|_w$ is the wall shear stress. The number of grid points (degrees of freedom) N scales as $N \approx Re^2$ (Ref. 11), which is nearly the same as for DNS. The classical remedy to this problem is to modify the subgrid model, by means of the following:

1) Modification of damping functions $\mathcal{D}$ that act as regularization prefactors to ν_k, such that $\nu_k = \mathcal{D}\nu_k$, is the first method. Typically, $\mathcal{D} = \{1 - \exp[-(\beta y^+)^3]\}^{1/2}$, where $y^+ = u_\tau y/\nu$.

2) The second modification is dynamic modeling based on Germanos identity $\boldsymbol{L} = \boldsymbol{T} - \tilde{\boldsymbol{B}}$ (Refs. 19 and 20), in which $\boldsymbol{L} = \overline{\bar{\boldsymbol{v}}\otimes\bar{\boldsymbol{v}}} - \bar{\bar{\boldsymbol{v}}}\otimes\bar{\bar{\boldsymbol{v}}}$ and $\boldsymbol{T} = \overline{\boldsymbol{v}\otimes\boldsymbol{v}} - \bar{\bar{\boldsymbol{v}}}\otimes\bar{\bar{\boldsymbol{v}}}$. By assuming that $\boldsymbol{B}$ and $\boldsymbol{T}$ can be closed with models of the same functional form, that is, $\boldsymbol{B} = -2c_D\Delta^2\|\bar{\boldsymbol{D}}\|\bar{\boldsymbol{D}}$ and $\boldsymbol{T} = -2c_D\tilde{\Delta}^2\|\bar{\bar{\boldsymbol{D}}}\|\bar{\bar{\boldsymbol{D}}}$, we now have that $\boldsymbol{L}_D = c_D\boldsymbol{X} - c_D\bar{\boldsymbol{Y}}$, where $\boldsymbol{X} = -2\tilde{\Delta}^2\|\bar{\bar{\boldsymbol{D}}}\|\bar{\bar{\boldsymbol{D}}}$ and $\boldsymbol{Y} = -2\tilde{\Delta}^2\|\bar{\bar{\boldsymbol{D}}}\|\bar{\bar{\boldsymbol{D}}}$, respectively. Hence, in the least-squares sense we have $c_D = \boldsymbol{M}\cdot\boldsymbol{L}/\boldsymbol{M}\cdot\boldsymbol{M}$, where $\boldsymbol{M} = \boldsymbol{X} - \bar{\boldsymbol{Y}}$. If the underlying model for $\boldsymbol{B}$ is based on the SMG model, [Eq. (5)], this approach will be referred to as the DSMG model.

3) The third dynamic modeling modification is based on the self-similarity between $\boldsymbol{B}$ and $\boldsymbol{L} = \overline{\bar{\boldsymbol{v}}\otimes\bar{\boldsymbol{v}}} - \bar{\bar{\boldsymbol{v}}}\otimes\bar{\bar{\boldsymbol{v}}}$ (Refs. 22 and 23). This can be used to evaluate the coefficient c_k and c_ε in the OEEVM [Eq. (5)]. Bounds for c_k and c_ε are determined from the realizability constraints. If the underlying model for $\boldsymbol{B}$ is based on the OEEVM model [Eq. (5)], this approach will be referred to as the LDKM model.

Alternatively we can use wall models. The simplest wall models are based on analytical expressions for the wall shear stress τ_w and

they provide an algebraic relationship between the local wall shear stress and the tangential velocities at the first off-wall nodes. Such algebraic models all imply the logarithmic law of the wall for the mean velocity, which is not generally valid in complex flows. The equations governing for the wall layer can be approximated by[4]

$$\partial_y[\nu(\partial_y \bar{v}_i) - B_{iy}] = f_i, \qquad f_i = \partial_i \bar{p} + \partial_t \bar{v}_i + \partial_j(\bar{v}_i \bar{v}_j) \quad (9)$$

Assuming that $f_i = \partial_i \bar{p}$, Eq. (9) can be integrated analytically to give the law of the wall,

$$\bar{v}^+ = \begin{cases} y^+ + \dfrac{y^+}{2u_\tau^2}\partial_i \bar{p} & \text{if} \quad y^+ \le y_0^+ \\ & y_0^+ = -\dfrac{1}{\kappa'} W[-\kappa' \cdot \exp(-B\kappa)] \\ \dfrac{1}{\kappa}\ell_n|y^+| + \dfrac{y^+}{\kappa u_\tau^2}\partial_i \bar{p} + B & \text{if} \quad y^+ > y_0^+ \end{cases} \quad (10)$$

where $\kappa \approx 0.41$ is the von Kármán constant, $B \approx 5.2$, $\kappa' = \kappa[1 - \partial p/\partial y(1/\kappa u_\tau^2 - 1/2u_\tau)]$ and W is the Lambert's W function.* Note that if $\partial_i \bar{p} = 0$ the classical law of the wall is recovered. For the full case, Eq. (9) has to be solved numerically. This approach has been used by Wang[28] and by Wang and Moin,[29] in which Eq. (9) is solved on an embedded near-wall grid to determine τ_w, using a mixing length model. Alternatively, Eq. (10) can be used to modify the subgrid model by adding a subgrid wall viscosity ν_{BC} to the viscosity ν on the wall so that the effective viscosity $\nu + \nu_{BC}$ becomes

$$\nu + \nu_{BC} = \tau_w/(\partial v_y/\partial y)_P = u_\tau y_{y,P} \big/ v^+_{y,P} \quad (11)$$

where the subscript P denotes that the quantity is to be evaluated at the first grid point away from the wall. This model can, in principle, be combined with any other subgrid model, and in the notation $+WM$ will be added to the baseline subgrid model name.

III. Alternative LES

In this section we present some of the more promising alternative approaches to conventional LES.

A. Detatched-Eddy Simulation

As an alternative to model ν_k using k, as working variable as in Eq. (5), we can instead model ν_k by its own transport equation. The most well-known transport equation model for ν_k is probably that of Spalart–Allmaras,[30] in which $\nu_k = f_{v1}\tilde{\nu}$, where

$$\partial_t(\tilde{\nu}) + \nabla \cdot (\tilde{\nu}\boldsymbol{v}) = c_{b1}\tilde{S}\tilde{\nu} + \nabla \cdot \{[(\nu + \tilde{\nu})/\sigma]\nabla\tilde{\nu}\} + (c_{b2}/\sigma)(\nabla\tilde{\nu})^2 - c_{w1} f_w(\tilde{\nu}/\tilde{d})^2 \quad (12)$$

where $f_{v1} = \chi^3/(\chi^3 + c_{v1}^3)$, $\chi = \tilde{\nu}/\nu$, $\tilde{D} = |\bar{\boldsymbol{D}}| + \tilde{\nu} f_{v2}/\kappa^2\tilde{d}^2$, $f_w = g[(1 + c_{w3}^6)/(g^6 + c_{w3}^6)]^{1/6}$, $f_{v2} = 1 - \chi/(1 + \chi f_{v1})$, $r = \tilde{\nu}/\tilde{D}\kappa^2\tilde{d}^2$, $g = r + c_{w2}(r^6 - r)$, and $\tilde{d} = \min(y, c_{DES}\Delta)$. The model coefficients are calibrated in simple homogeneous and free flows and take the values: $c_{b1} = 0.135$, $c_{b2} = 0.62$, $\sigma = 2/3$, $\kappa = 0.41$, $c_{w1} = 3.24$, $c_{w2} = 0.3$, $c_{w3} = 2.0$, $c_{v1} = 7.10$, and $c_{DES} = 0.65$. This approach is commonly referred to as detatched-eddy simulation[31,32] but can also be interpreted as a LES model using the modified Spalart–Allmaras turbulence model as the subgrid (eddy-viscosity) model. DES suffers from same drawbacks as the other functional models (compare Sec. II.A).

*Data available online at http://mathworld.wolfram.com/lambertsw-function.html.

B. Monotone Integrated LES

In monotone-integrated LES (MILES) the discretization effectively filters the NSE across the grid using an anisotropic kernel. When founding MILES on concepts like the flux corrected transport (FCT),[33,34] the functional reconstruction of the convective fluxes is done using a flux-limiting method combining a high-order flux function with a low-order dispersion-free flux function using a nonlinear flux-limiter Γ. Moreover, the functional reconstruction of the viscous fluxes is typically performed using linear or cubic interpolation. Similar approaches have been used by others, for example, Refs. 34–39, and are discussed in greater detail in Ref. 9 and references therein. Physical considerations motivating MILES have been presented in Ref. 34, and some formal properties were recently documented using databases of free and wall-bounded flows.[39] The modified equations provide the most suitable platform for comparing MILES and LES, and following Fureby and Grinstein[34] the implicit subgrid model can, in a finite volume context, be formulated as

$$\boldsymbol{B} = \boldsymbol{C}(\nabla\boldsymbol{v})^T + (\nabla\boldsymbol{v})\boldsymbol{C}^T + \chi^2(\nabla\boldsymbol{v})\boldsymbol{d} \otimes (\nabla\boldsymbol{v})\boldsymbol{d} \quad (13)$$

where $\boldsymbol{C} = \chi(\boldsymbol{v} \otimes \boldsymbol{d})$, $\chi = \frac{1}{2}(1 - \Gamma)(\beta^- - \beta^+)$, and $\beta^\pm = \frac{1}{2}(\boldsymbol{v}_f \cdot \mathrm{d}\boldsymbol{A} \pm |\boldsymbol{v}_f \cdot \mathrm{d}\boldsymbol{A}|)/|\boldsymbol{v}_f \cdot \mathrm{d}\boldsymbol{A}|$. In particular, we note that in smooth regions $\Gamma = 1$ implies that $\chi = 0$ and $\boldsymbol{C} = \boldsymbol{0}$ and $\boldsymbol{B} = \boldsymbol{0}$. The implicit subgrid stress tensor can be decomposed into $\boldsymbol{B}^{(1)} = \boldsymbol{C}(\nabla\boldsymbol{v})^T + (\nabla\boldsymbol{v})\boldsymbol{C}^T$ and $\boldsymbol{B}^{(2)} = \chi^2(\nabla\boldsymbol{v})\boldsymbol{d} \otimes (\nabla\boldsymbol{v})\boldsymbol{d}$, in which the former is a tensor-valued eddy-viscosity model with $\boldsymbol{C}$ the eddy-viscosity tensor, whereas the latter is of a form equivalent to the first part of the mixed model [Eq. (7)]. In MILES the eigenvectors of $\boldsymbol{B}$ and $\bar{\boldsymbol{D}}$ are not parallel to each other, and the model partially complies with Eq. (3).

C. Approximate Deconvolution Model

In the approximate deconvolution model (ADM) of Adams and Stolz[40] and Stolz et al.,[41] an effort is made to close Eq. (1) in a systematic manner by taking also the commutation error term into account. The low-wave-number part of the unfiltered fields is reconstructed by inverting the filtering. Following the terminology of Stolz et al.,[41] we differentiate between the soft deconvolution problem, which corresponds to reconstructing the unfiltered fields at scales larger than Δ, and the hard deconvolution problem, which corresponds to modeling the effects of the scales below Δ. The soft deconvolution problem is best solved using regularization procedures of, for example, van Cittert[42] or Tikhonov and Arsenin,[43] resulting in $\boldsymbol{v} \approx \bar{\boldsymbol{v}} + (\bar{\boldsymbol{v}} - \bar{\bar{\boldsymbol{v}}}) + (\bar{\boldsymbol{v}} - 2\bar{\bar{\boldsymbol{v}}} + \bar{\bar{\bar{\boldsymbol{v}}}}) + \ldots$, which can be used to close

$$\partial_t(\bar{\boldsymbol{v}}) + \nabla \cdot (\bar{\boldsymbol{v}} \otimes \bar{\boldsymbol{v}}) = -\nabla\bar{p} + \nabla \cdot (\nu\nabla\bar{\boldsymbol{v}}) - \nabla \cdot (\overline{\boldsymbol{v} \otimes \boldsymbol{v}} - \bar{\boldsymbol{v}} \otimes \bar{\boldsymbol{v}}) + [G*, \nabla](\boldsymbol{v} \otimes \boldsymbol{v} + p\boldsymbol{I} - \nu\nabla\boldsymbol{v}) \quad (14)$$

whereas the hard deconvolution problem, essentially representing forward scatter of energy from the resolved scales to the unresolved scales, is closed using using either an eddy-viscosity approximation restricted to the smallest resolved scales ($\nu := \nu + c_D\Delta^2\|\boldsymbol{D}'\|$, where $\boldsymbol{D}'$ is evaluted from $\boldsymbol{v}'$) or preferably by the penalty-type approach of Stolz and Adams.[41]

IV. Emerging LES Approaches

In this section we present two emerging LES approaches that potentially have some advantages over other conventional and alternative LES approaches.

A. The Two-Level Simulation LES Model

In the two-level simulation (TLS) approach of Kemenov and Menon,[44,45] both the resolved and subgrid scales of motion are explicitly simulated. Regardless of how this approach is implemented, it is clear that if both the resolved and subgrid scales are simulated in three dimensions this method is no different from DNS and hence far too expensive for engineering flow problems. However, inspired by Kerstein,[46] Kemenov and Menon developed an approach in which the large scales evolve on an ordinary LES grid under the action of the subgrid force $\boldsymbol{f}^{res}$. The small scales evolve on locally embedded one-dimensional grids. This reduction in dimensionality permits the

TLS approach to be computationally feasible and generally applicable to high-Reynolds-number flows in complex geometries.

In this framework the decomposition into resolved and subgrid components (i.e., $\boldsymbol{v}=\bar{\boldsymbol{v}}+\boldsymbol{v}'$) is substituted into the NSE giving the baseline TLS equations:

$$\partial_t(\bar{\boldsymbol{v}})+\nabla\cdot[(\bar{\boldsymbol{v}}+\boldsymbol{v}')\otimes(\bar{\boldsymbol{v}}+\boldsymbol{v}')]=-\nabla\bar{p}+\nabla\cdot\bar{\boldsymbol{S}}+\boldsymbol{f}^{\mathrm{sgs}}$$

$$\nabla\cdot\bar{\boldsymbol{v}}=0$$

$$\partial_t(\boldsymbol{v}')+\nabla\cdot[(\bar{\boldsymbol{v}}+\boldsymbol{v}')\otimes(\bar{\boldsymbol{v}}+\boldsymbol{v}')]=-\nabla p'+\nabla\cdot\boldsymbol{S}'+\boldsymbol{f}^{\mathrm{res}}$$

$$\nabla\cdot\boldsymbol{v}'=0 \tag{15}$$

where $\boldsymbol{f}^{\mathrm{sgs}}=-\partial_t(\boldsymbol{v}')-\nabla p'+\nabla\cdot\boldsymbol{S}'$ and $\boldsymbol{f}^{\mathrm{res}}=-\partial_t(\bar{\boldsymbol{v}})-\nabla\bar{p}+\nabla\cdot\bar{\boldsymbol{S}}$ are the subgrid and resolved forcing terms, respectively. Note that, in contrast to conventional LES, the TLS approach is inherently free from issues associated with the commutation errors, which is an issue near walls and on nonuniform grids.[12] Solving the full system (15) is equivalent to performing a DNS, and therefore additional simplifications of (15) and associated modeling are necessary. In the TLS (15_2) is simplified in the sense that $\boldsymbol{v}'$ is modeled as a family of one-dimensional vector fields defined on one-dimensional lines embedded in the three-dimensional domain, that is, $\boldsymbol{v}'=v'_i(s_\ell,t)\boldsymbol{e}_i^\ell=v'_{i,\ell}\boldsymbol{e}_i^\ell$, where $i=1,\ldots,3$; $\ell=1,\ldots,N$, where N is the total number of one-dimensional lines (which can be several thousands), s_ℓ is the (arc length) coordinate along the line ℓ, and $\boldsymbol{e}_i^\ell$ is the unit base vector of that line. This formulation is thus gemetrically versatile in that the lines ℓ can take any shape. In addition it is assumed that the derivatives of the subgrid-scale fields $\boldsymbol{v}'$ in all three directions are equal. Applying this to Eq. (15_1) leads to

$$\partial_t(\bar{\boldsymbol{v}})+\nabla\cdot[(\bar{\boldsymbol{v}}+\langle\boldsymbol{v}'\rangle)\otimes(\bar{\boldsymbol{v}}+\langle\boldsymbol{v}'\rangle)]$$

$$=-\nabla\bar{p}+\nabla\cdot\bar{\boldsymbol{S}}+\langle\boldsymbol{f}^{\mathrm{sgs}}\rangle,\qquad\nabla\cdot\bar{\boldsymbol{v}}=0$$

$$\partial_t\left(v'_{i,\ell}\boldsymbol{e}_i^\ell\right)+\nabla\cdot\left[\left(\bar{\boldsymbol{v}}+v'_{i,\ell}\boldsymbol{e}_i^\ell\right)\otimes\left(\bar{\boldsymbol{v}}+v'_{i,\ell}\boldsymbol{e}_i^\ell\right)\right]$$

$$=-\nabla p'+\nabla\cdot\boldsymbol{S}'+\boldsymbol{f}^{\mathrm{res}},\qquad\nabla\cdot\left(v'_{i,\ell}\boldsymbol{e}_i^\ell\right)=0 \tag{16}$$

where $\langle\cdot\rangle$ in Eq. (16_1) denotes the local averaging operation required when transforming the small-scale fields back onto the three-dimensional domain. When the orientation coincides with the orientation of the LES grid, the resulting one-dimensional equations become particularly simple.[45] Boundary conditions are then naturally imposed on $\boldsymbol{v}'$ at the three-dimensional domain boundaries.

B. Homogenization-Based LES Model

With the intent of deriving improved subgrid models, particularly for high-Reynolds-number wall-bounded flows, Persson et al.[47] use homogenization by multiple-scales expansion[48] to derive the LES model. To this end, they introduce the two-scale expansion,

$$\boldsymbol{v}=\boldsymbol{v}_\delta+\boldsymbol{v}'_\delta=\bar{\boldsymbol{v}}(\boldsymbol{x},t)+\sum_{k=1}^{\infty}\delta^k\boldsymbol{v}_k(\boldsymbol{x},t;\xi,\tau)+\boldsymbol{v}'_\delta(\xi,\tau)$$

$$p=\delta^{-2}p_{-2}+\delta^{-1}p_{-1}+\bar{p}+\tilde{p}+\sum_{k=1}^{\infty}\delta^k p_k(\boldsymbol{x},t;\xi,\tau) \tag{17}$$

where $\bar{\boldsymbol{v}}(\boldsymbol{x},t)=\boldsymbol{v}_0(\boldsymbol{x},t)$ and $\bar{p}=\bar{p}(x,t)$ denote the LES variables, whereas $\tilde{p}=\tilde{p}(\xi,\tau)$ is the Lagrange multiplier necessary to guarantee that $\nabla_\xi\cdot\boldsymbol{v}_1=0$. For high Reynolds numbers not all eddy scales can be expected to be resolved, and hence $\boldsymbol{v}'_\delta$ is represented by the predefined stochastic process $\boldsymbol{w}=\boldsymbol{w}(\xi,\tau)$ such that $\boldsymbol{v}'_\delta=\delta^{-1}\boldsymbol{v}_{-1}=\delta^{-1}\boldsymbol{w}(\xi,\tau)$. Here, $\boldsymbol{\xi}$ and τ denote the subgrid variables. From the scaling symmetries of the NSE, the only natural choice for the subgrid variables is $\tau=t/\delta^2$ and $\xi=\boldsymbol{x}/\delta$. Formal expansion of the NSE using Eq. (17) and the chain rule of differentiation results in a cascade of equations [Eq. (13) in Ref. 47], which can be used to formally derive equations for the large and small scales, respectively, by identifying coefficients for the scale parameter δ. This yields the LES equations

$$\nabla_x\cdot\bar{\boldsymbol{v}}=0,\qquad\partial_t\bar{\boldsymbol{v}}+\nabla_x\cdot(\bar{\boldsymbol{v}}\otimes\bar{\boldsymbol{v}})=-\nabla_x\bar{p}+\nabla_x\cdot(\nu\nabla_x\bar{\boldsymbol{v}}-\boldsymbol{B}) \tag{18}$$

where $\boldsymbol{B}=\overline{\boldsymbol{w}\otimes\boldsymbol{v}_1}+\overline{\boldsymbol{v}_1\otimes\boldsymbol{w}}$ is the subgrid stress tensor and the microstructure problem

$$\nabla_\xi\cdot\boldsymbol{v}_1=0$$

$$\partial_\tau\boldsymbol{v}_1+\nabla_\xi\cdot(\boldsymbol{w}\otimes\boldsymbol{v}_1+\boldsymbol{v}_1\otimes\boldsymbol{w})=-\nabla_\xi\tilde{p}+\nu\nabla_\xi^2\boldsymbol{v}_1-\nabla_x\cdot(\boldsymbol{w}\otimes\bar{\boldsymbol{v}}) \tag{19}$$

describing the small-scale flow physics. Furthermore, the analysis also implies that the stochastic process $\boldsymbol{w}$ must obey $\partial_\tau\boldsymbol{w}+\nabla_\xi\cdot(\boldsymbol{w}\otimes\boldsymbol{w})=\nu\nabla_\xi^2\boldsymbol{w}-\nabla_\xi p_{-2}$, with zero mean over each LES cell. The fact that $\boldsymbol{v}_1$ depends only parametrically on $\nabla_x\bar{\boldsymbol{v}}$, as evident from Eq. (19), allowed Persson et al.[47] to derive solutions to Eq. (19) by superposition so that

$$B_{ij}=A_{ijkl}\partial_{x^l}\bar{v}^k\qquad\text{with}\qquad A_{ijkl}=\overline{w^i\chi_{kl}^{\ j}+w^j\chi_{kl}^{\ i}} \tag{20}$$

where A_{ijkl} is a fourth-rank (eddy-viscosity) tensor. In Ref. 47 an attempt was made to estimate A_{ijkl} based on choosing $\boldsymbol{w}$ to comply with the Kolmogorov subrange spectrum $E(\boldsymbol{k})=c_K\varepsilon^{2/3}\boldsymbol{k}^{-5/3}$ and to assume negligible subgrid transport. Accordingly,

$$A_{hjkl}=(2\pi)^{-\frac{11}{3}}c_K c_\varepsilon^{\frac{2}{3}}\left(\Delta\sqrt{k}\right)^2\nu^{-1}\tilde{A}_{hjkl} \tag{21}$$

where $\tilde{A}_{hjkl}=\tilde{A}_{hjkl}(\Delta)$ is a symmetric tensor expressing the local anisotropic grid scaling. This model will henceforth be referred to as HOM. The main advantage of HOM is that the eigenvectors of $\boldsymbol{B}$ and $\bar{\boldsymbol{D}}$ are not parallel to each other and that the model still is of the eddy-viscosity form, providing 1) easy implementation and 2) a way of handling nonuniform grids.

V. Numerical Methods

The application of LES to engineering problems requires not only good subgrid turbulence models and fast computers, but also accurate and robust numerical methods. Unstructured grids are desirable because the time required for generating unstructured grids is usually considerably lower than for block-structured grids. To this end, the finite volume (FV) method is appropriate. However, nondissipative schemes that conserve not only momentum but also kinetic energy are required for successful LES computations. Discrete conservation of kinetic energy, in the sence that the integral

$$\int_{\partial D}\left[\tfrac{1}{2}\bar{\boldsymbol{v}}^2\bar{\boldsymbol{v}}+(\bar{p}\boldsymbol{I}-2\nu\bar{\boldsymbol{D}}+\boldsymbol{B})\bar{\boldsymbol{v}}\right]\cdot\mathrm{d}\boldsymbol{A}$$

is bounded (with $\mathrm{d}\boldsymbol{A}$ an area element and D a control volume), ensures robustness without numerical dissipation that compromises accuracy.

In the computational results to be presented, two codes have been used. FOAM[49] is used by FOI and is here used for the channel flow and prolate spheroid LES computations. FOAM is based on a cell-centered, unstructured FV method for which different numerical schemes can be selected. For LES a second-order-accurate scheme (based on central differencing for both convective and diffusive terms) is used, whereas for MILES an FTC scheme is used for the convective terms and central differencing for the diffusive terms. To decouple the pressure-velocity system, a Poisson equation, derived from the discretized continuity and momentum equations, is constructed for $\bar{p}$. The scalar equations are solved in sequence with iteration over the coupling terms. The segregated approach results in a Courant–Friedrichs–Lewy (CFL)-number restriction of CFL$<$0.5, but for LES we typically require that CFL$<$0.3. FOAM is parallelized using PVM or message-passing interface (MPI) and provides scalability of 95% for 100 processors with superlinear speedup for a smaller number of processors.

The GaTech code is based on a boundary-conforming structured FV scheme that is fourth-order accurate in space and second-order accurate in time. For the channel flow calculations an incompressible solver is used, where the one-dimensional TLS lines are farmed out to the slave processors, whereas for the axisymmetric hill computations a compressible solver is employed. This compressible solver is very efficient on parallel architectures enabling these simulations. The computational domains are distributed in parallel using the MPI standard. The implementation and optimization of the TLS model is not straightforward but is described in detail in Ref. 46.

VI. Turbulent Channel Flow

The first test case to be discussed is the fully developed turbulent channel flow at bulk Reynolds-numbers between $Re = 8 \times 10^3$ and 4×10^4. The channel is confined between two perfectly smooth parallel plates $2h$ apart, where h is the channel half-width. The flow is driven by a fixed mass flow in the streamwise $\boldsymbol{e}_x$ direction defining the mean velocity $\langle \bar{\boldsymbol{v}} \rangle$. No-slip conditions are used in the cross-stream $\boldsymbol{e}_y$ direction, and periodic conditions are used in the spanwise $\boldsymbol{e}_z$ direction. As initial conditions a parabolic $\bar{\boldsymbol{v}}$ distribution is used. After reaching a statistically steady state, the runs were continued for a sufficient number of time units (h/u_τ) to collect the first- and second-order statistical moments used for comparison with DNS and experimental data. For $Re_\tau = 395$ and 590 DNS data, employing $256 \times 193 \times 192$ and $384 \times 257 \times 384$ grid points are available from Moser et al.,[50] and for $Re_\tau = 1.8 \times 10^3$ experimental data are available from Wei and Willmarth.[51] The physical size of the channels are $6h \times 2h \times 3h$ in the streamwise, cross-stream, and spanwise directions, respectively. All LES computations with the exception of the TLS model use 60^3 grids with uniform spacing in the stream- and spanwise directions, whereas geometrical progression is used in the $\boldsymbol{e}_y$ direction to cluster the grid toward the walls. In terms of + units, the resolution varies between $(\Delta x^+, \Delta y^+, \Delta z^+) = (40, 0.3, 20)$ and $(180, 2, 90)$, respectively. The TLS model employ a $32 \times 40 \times 32$ grid with $(\Delta x^+, \Delta y^+, \Delta z^+)$ between (78, 13, 39) and (116, 19, 60), respectively, along with $237 \times 257 \times 257$ embedded one-dimensional lines in the wall-normal, streamwise, and spanwise directions.

Figure 1 shows the main flow features of the channel flow in terms of vortex lines, contours of $\langle \bar{v}_x \rangle$, and isosurfaces of the second invariant of the velocity gradient $Q = \frac{1}{2}(\|\boldsymbol{W}\|^2 - \|\boldsymbol{D}\|^2)$. The location of a vortex line is given by the equation $\mathrm{d}\boldsymbol{x}/\mathrm{d}s = \boldsymbol{\omega}/|\bar{\boldsymbol{\omega}}|$, where s is the distance along the vortex line. This equation is integrated using a third-order Runge–Kutta method together with a second-order linear interpolation scheme to compute $\bar{\boldsymbol{\omega}}$ from the grid points. By correlating isosurfaces of Q with $\bar{\boldsymbol{v}}$ close to the wall, it is found that vortices above the low-speed streaks are often ejected away from the wall, as found in experiments and LES and DNS, producing hairpin vortices stretched by the ambient shear. By this mechanism vorticity produced in the viscous region is advected into the boundary layer, making it turbulent. As in DNS and other LES the hairpin vortices are often asymmetric, with one leg stronger than the other. The spanwise resolution is found more important for the accurate prediction of the coherent structure dynamics than the streamwise resolution. The wall-normal resolution is important for the accurate prediction of the wall shear stress τ_w, which, in turn, is important for making correct estimates of the drag.

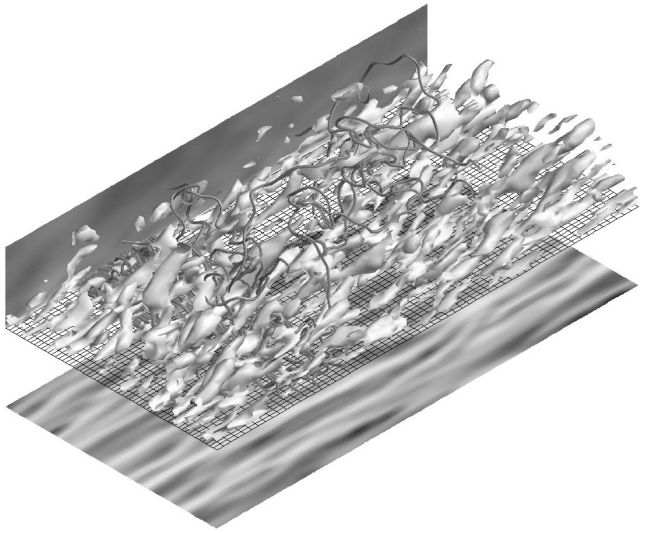

Fig. 1 Perspective of fully developed turbulent channel flow at $Re_\tau = 590$.

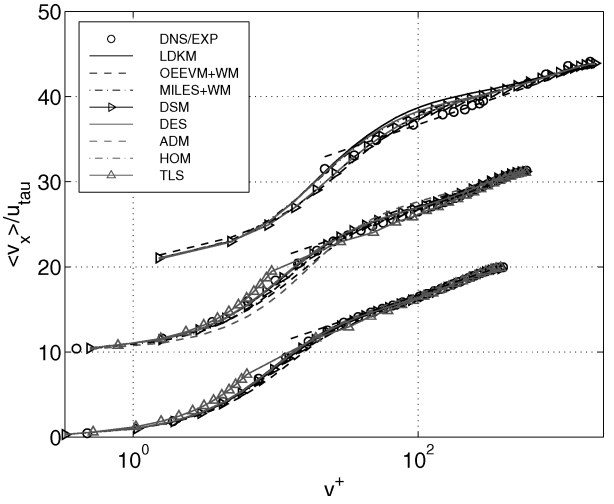

Fig. 2 Time-averaged streamwise velocity profiles ($\langle v_x \rangle^+$) at $Re_\tau = 395$, 590, and 1800. The results for $Re_\tau = 590$ and 1800 are shifted 10 and 20 units, respectively, in the vertical direction.

In Fig. 2 we compare our LES predictions of the time-averaged streamwise velocity $\langle \bar{v}_x \rangle$ (integrated over x and z) with the DNS and experimental data.[50,51] For $Re_\tau = 395$ and 590 all LES models examined show good agreement with the DNS data across the channel, with the DSM providing the best overall agreement with the DNS data. The TLS model predicts slightly higher values of $\langle \bar{v}_x \rangle^+ = \langle \bar{v}_x \rangle / u_\tau$ in the buffer region $(10 < y^+ < 30)$, which might be caused by the coarse baseline grid. For $R_\tau = 590$ the ADM model underpredicts $\langle \bar{v}_x \rangle^+$ in the viscous sublayer $(y^+ < 10)$ and in the buffer region and overpredicts $\langle \bar{v}_x \rangle / v^+$ in the logarithmic region $(30 \langle y^+ \rangle 300)$. The reason for this inadequate behavior might be insufficient dissipation, which here is related only to the smallest resolved scales. For $Re_\tau = 1.8 \times 10^3$ we still find reasonable agreement between the LES and the experimental data, but with larger scatter in the LES data. The eddy-viscosity models (OEEVM + WM, DES and LDKM) all tend to overpredict $\langle \bar{v}_x \rangle^+$ in the beginning of the logarithmic region and underpredict it at the end of the logarithmic region. The log-law $\langle \bar{v}_x \rangle^+ = \kappa^{-1} \ell_n(y^+) + B$ is generally well predicted with $B \approx 5.2 \pm 0.1$ and $\kappa \approx 0.41 \pm 0.01$. The predictions of the skin-friction coefficient C_f, on the other hand are unsatisfactory: for $Re = 395$ the models underpredict C_f by about 1%, whereas at $Re = 1.8 \times 10^3$ C_f is underpredicted by between 10 and 20% depending on model.

In Fig. 3 we compare our LES predictions of the streamwise resolvable rms-velocity fluctuation $\bar{v}_x'^+ = \bar{v}_x'/u_\tau$ (integrated over x and z), where $\bar{v}_x' = \sqrt{[\langle (\bar{v}_x - \langle \bar{v}_x \rangle)^2 \rangle]}$, with the DNS and experimental data.[50,51] For $Re_\tau = 395$ all LES models show good agreement with the DNS data over the channel, but for $Re_\tau = 590$ the scatter between the LES model predictions increases. Best agreement is obtained with the TLS model, which correctly predicts the location $(y^+ \approx 15)$ and the peak value, but produces a broader profile. The worst agreement is found for ADM and DSM, which overpredicts the peak value of $\bar{v}_x'^+$ by almost 10% and produces a profile that is shifted away from the wall. Most other models (OEEVM + WM, LDKM, MILES, and DES) tend to overpredict the peak value by between 2 and 5%. For $Re_\tau = 1.8 \times 10^3$ the agreement between LES and the experimental data is only fair; best agreement is obtained with MILES and DSM, and worst agreement is obtained with the

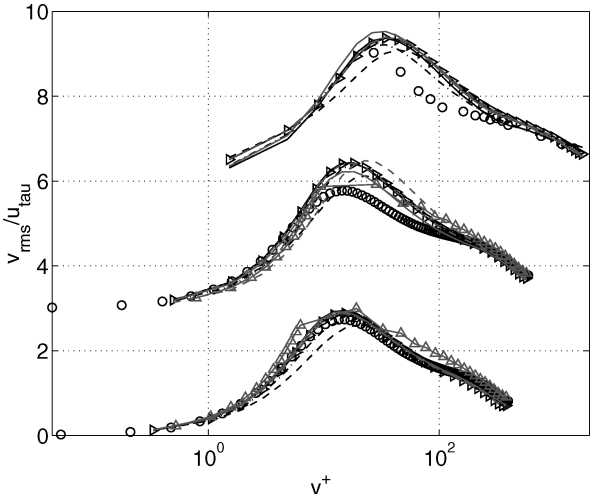

Fig. 3 Rms-velocity fluctuation profiles $v_{\rm rms}$ at $Re_\tau = 395$, 590, and 1800. Note that the results for $Re_\tau = 590$ and 1800 are shifted three and six units in the vertical direction. Legend as in Fig. 2.

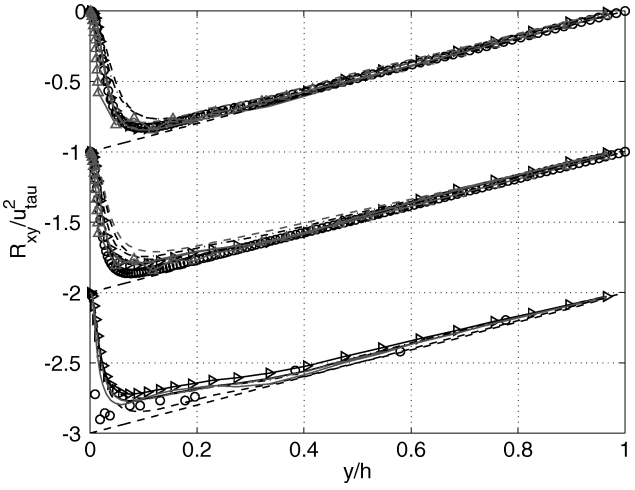

Fig. 4 Reynolds shear stress profiles R_{xy} at $Re_\tau = 395$ and 590, respectively. Note that the data for $Re_\tau = 590$ and 1800 are shifted one and two units in the vertical direction. Legend as in Fig. 2.

DES model. The overall trend is that the predicted profiles are wider than the measured profiles, and that the predicted profiles are shifted away from the wall.

In Fig. 4 we compare our LES predictions of the resolvable shear stress $\bar{R}_{xy} = \langle \bar{v}'_x \bar{v}'_y \rangle$ with DNS and experimental data.[50,51] Both R_{xy} and $\bar{R}_{xy}$ profiles are bounded by $u_\tau^2 y/h$, which therefore constitute an upper/lower bound for R_{xy}. Hence, as the Re_τ number increases, the resolved fraction (i.e., $\bar{R}_{xy}$) decreases, which therefore emphasizes the fact that the demands on the subgrid model increase with increasing Reynolds number given a fixed resolution. For $Re_\tau = 395$ good agreement with the DNS data is found for all models. DES and MILES show somewhat lower values of $\bar{R}_{xy}$ than the other models. For $Re_\tau = 590$ the scatter between the $\bar{R}_{xy}$ profiles is larger, but the shapes are generally well reproduced. For $Re_\tau = 1.8 \times 10^3$ this trend is continued, with $\bar{R}_{xy}$ covering a lower fraction of R_{xy} than for $Re_\tau = 590$ and 395.

VII. Flow over an Axisymmetric Hill

In our attempts to extend the use of LES to engineering problems of practical interest, a particularly interesting issue is that of flows over curved surfaces, typically involving three-dimensional unsteady separation and reattachment. High-Reynolds-number flows of this kind are of considerable interest because of their relevance for naval and other vehicle applications. CFD approaches using RANS models, experimentally based model coefficients, and advanced steady-state flow codes are usually unable to predict such flows with sufficient accuracy. To this end, an interesting flow configuration, experimentally investigated by Simpson et al.,[52] and Simpson,[53] is that of the flow over an axisymmetric hill of hill height $H = 2\delta$ and δ, where δ is the boundary-layer thickness. In Ref. 54 LES, using the LDKM subgrid model, have been applied to the same flow, and the results of the LES are compared to the detailed experimental measurements of Simpson.[53] These flows produce complex vortical structures with multiple separation and reattachment zones covering a large part of the lee side of the hill with the height of the hill strongly affecting the flowfield.

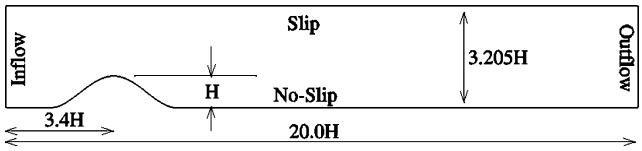

Fig. 5 Schematic of the computational domain.

Figure 5 presents the geometry of the axisymmetric hill case in the streamwise and wall-normal directions. The hill height is $H = 0.078$ m with the circular base of radius $R = 2H$. The zenith of the hill is about $3.4H$ downstream from the inflow boundary, and the computational domain extends $6H$ in the spanwise direction. The shape of the hill is defined analytically as

$$y(r) = H/6.04844[J_0(\Lambda)I_0(\Lambda r/R) - I_0(\Lambda)J_0(\Lambda r/R)] \quad (22)$$

where $\Lambda = 3.1926$, J_0 is the Bessel function of the first kind, and I_0 is the modified Bessel function of the first kind. The Reynolds number, based on H and the flow velocity ($v_0 = 27.5$ m/s), is about 1.3×10^5. Simulations have been conducted using different grids ranging between $128 \times 64 \times 64$ and $256 \times 128 \times 128$ cells. For these grids the minimum grid resolutions in the wall-normal direction are about 116 and 56 μm, respectively. The finer resolution is chosen so as to give enough grid points near the body surface to reasonably resolve the boundary layer and also the separation downstream of the hill. An estimate in terms of viscous wall units yields the minimum grid resolutions of $(\Delta x^+, \Delta y^+, \Delta z^+) = (24, 8, 200)$ and $(12, 4, 100)$, respectively. Grid clustering is employed in the near wall-region and on the lee side of the hill zenith. However, grid stretching was kept to a minimum, typically less than 4% in regions of high shear, to minimize stretching errors.

Simpson et al.[52] report profiles with the speed v_0 and with 0.1% freestream turbulence intensity, having a boundary-layer thickness of $\delta_{99} \approx 39$ mm and $Re_\theta \approx 7.3 \times 10^3$. Similar inflow profiles were used, in which a Gaussian random field (0.1% of the mean) is added to the inlet velocity profile in order to emulate the freestream turbulence. Accordingly, the subgrid turbulent kinetic energy at the inflow boundary is also initiated to that level. For this relatively low level of inflow turbulence, most of the subgrid kinetic energy k in the flow is therefore caused by the production in the boundary layer. At the upper boundary of the computational domain, slip conditions are enforced for the velocity and k, whereas wave-transmissive conditions are used for p. At the outlet boundary zero Neumann conditions are applied to all variables. At the lower wall, no-slip conditions are enforced for both the velocity and k, whereas compressible characteristic boundary conditions are used for p. To wash out the effects of the initial conditions, the simulations are allowed to evolve several flow-through times before any data are collected for analysis.

Figure 6 presents a comparison of the predicted mean surface streamline pattern with the experimental oil-flow pattern. Based on the mean and instantaneous surface streamline patterns, we find that the flow on the lee side of the bump is very complex and highly three-dimensional because of both streamwise and spanwise pressure gradients on the lee side. Complex vortical structures appear downstream of the zenith of the hill, where also multiple separations and stagnation points/regions can be seen. These regions are highly transient and do not show any (instantaneous) symmetry in the spanwise direction. The velocity (Fig. 5b in Ref. 54) suggests separation on the lee side that reattaches and separates. Compared to the experimental oil-flow visualizations (Fig. 6b), good qualitative and quantitative agreement can be found, with the experiments

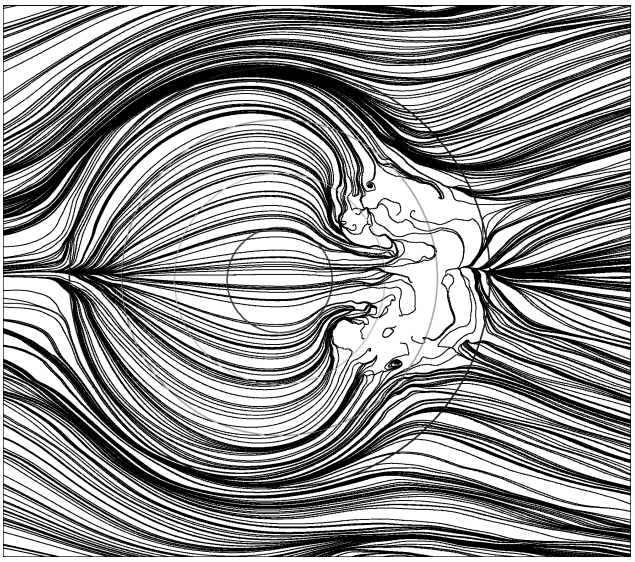

a)

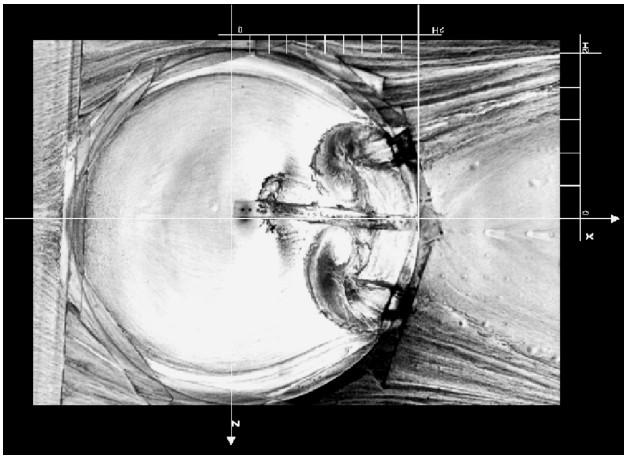

b)

Fig. 6 Oil-flow visualizations (using streamlines in the near-wall region) for the a) numerical study and b) experiments.

typically showing an unsteady complex pattern of multistage separation and reattachment. These vortical structures are formed because the fluid motion is embedded in a three-dimensional pressure gradient field, with the incoming flow accelerating both over the top and around the sides of the hill as a result of the favorable pressure gradient in both directions. The pressure-gradient magnitude decreases outward from the pressure minimum at the center plane. The flow decelerates on the lee side with the pressure reaching a maximum at the center plane just at the end of the hill. Moreover, the spanwise favorable pressure gradient in the front causes the flow to initially diverge around the hill, and on the lee side this gradient is adverse causing the side boundary layers to converge on the back of the hill.

Typical results for the (time-averaged) static-pressure coefficient $C_P = (\bar{p} - p_0)/(\tilde{p} - p_0)$, where $\bar{p}$ is the local static pressure, p_0 is the static reference pressure, and $\tilde{p}$ is the local total pressure, are presented and compared with the experimental measurement data in Fig. 7. There is good similarity in both features and magnitudes between the LES computations in Fig. 7a, and the experimental data in Fig. 7b. Both results show that as the boundary layer approaches the leading face of the hill the pressure, increases, but the increase is not large enough to cause separation. The pressure then decreases at the zenith of the hill as the flow accelerates over the hill. The peak pressure occurs exactly at the zenith of the hill, but the LES computations suggest a larger peak region than do the experimental measurements. Furthermore, the adverse pressure gradient begins later in the computations than in the experiments. This might be caused by the larger low-pressure region predicted on the zenith of

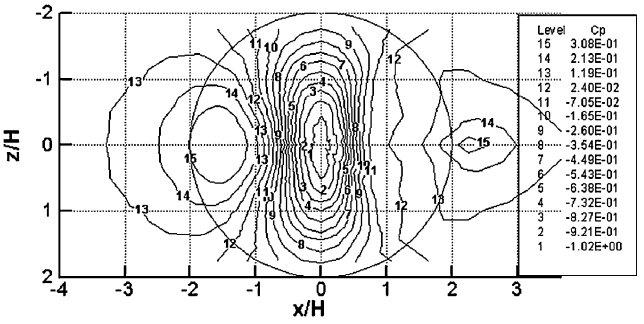

a) Measured

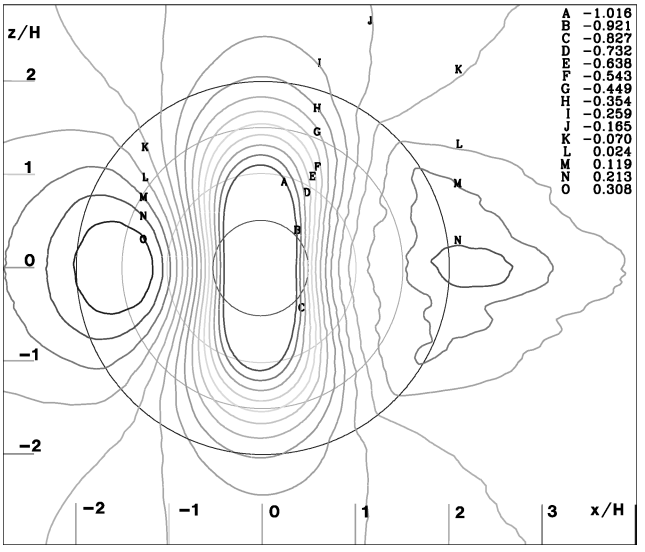

b) Predicted

Fig. 7 Static-pressure coefficients C_P contours over the hill surface.

the hill. In the spanwise direction, both LES and experiments show a symmetric pressure distribution as could be expected.

Figure 8 presents comparisons for the streamwise velocity and the resolved shear stresses, normalized by u_τ, at $3.69H$ downstream of the hill zenith for various spanwise locations on either side of the center plane. At this location the flow has reattached on the lower wall, and the turbulent boundary layer has reformed. The agreement between LES, using LDKM, and the experimental data is qualitatively and quantitatively good, considering the complexity of the flow and the difficulties associated with supergrid modeling. The magnitude of u_τ agrees well with the LES computations and the experiments, and the spanwise variation is also qualitatively similar. Both LES and experiments show that a viscous sublayer exists for $y^+ < 10$ and that a classical log-profile occurs between $10 < y^+ < 1000$. The predicted slope of the log profile is in good agreement with the well-known log law and the experimental data. In the wake region ($y^+ > 1000$) less good agreement between experimental data and the LES results is observed. This might be caused by different factors, but the most plausible issue is the lack of reliable inflow or boundary data with embedded dynamics and flow structures. The issue of supergrid modeling,[39] currently limits the usefulness of LES (and DNS), but as long as this is borne in mind LES is still a useful tool in engineering. Finally, we notice that the LES capture the detailed variation of the velocity in the spanwise direction, which is regarded as promising considering the complexity of the flow.

VIII. Flow over an Inclined Prolate Spheroid

Despite its simple geometry, the flow around an inclined prolate spheroid, Fig. 9, contains a rich gallery of complex three-dimensional flow features. The flow is here represented by streamribbons, contours of the vorticity magnitude $|\bar{\omega}|$, where $\bar{\omega} = \frac{1}{2}\nabla \times \bar{\nu}$ is the vorticity vector, at $x/L = 0.600$ and 0.772, respectively,

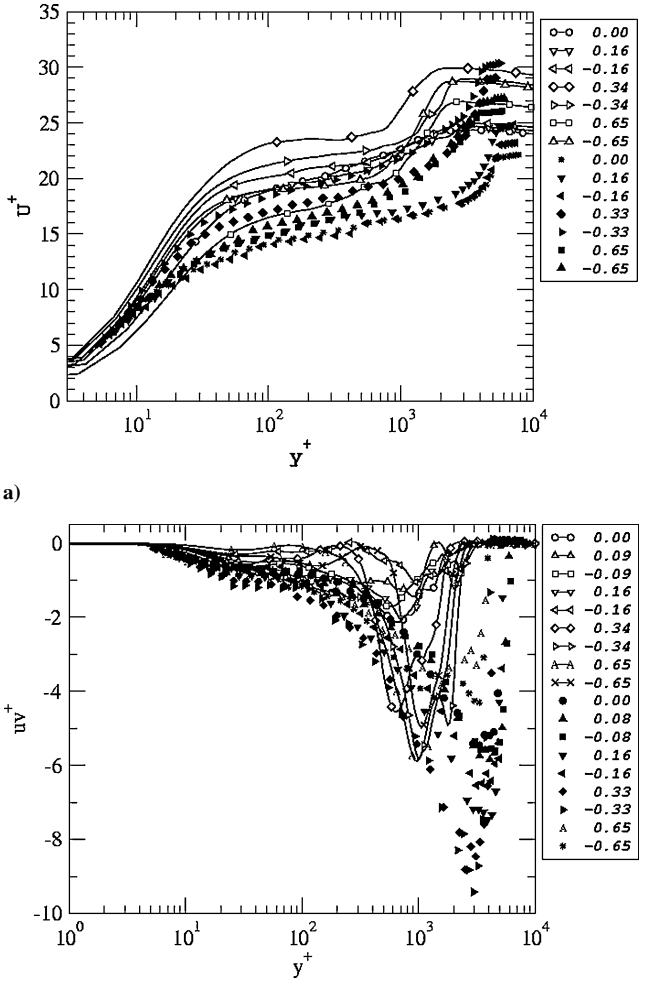

Fig. 8 Comparison of the predicted and measured velocity profiles at 3.69*H* downstream of the hill peak for various spanwise locations on either side of the center plane

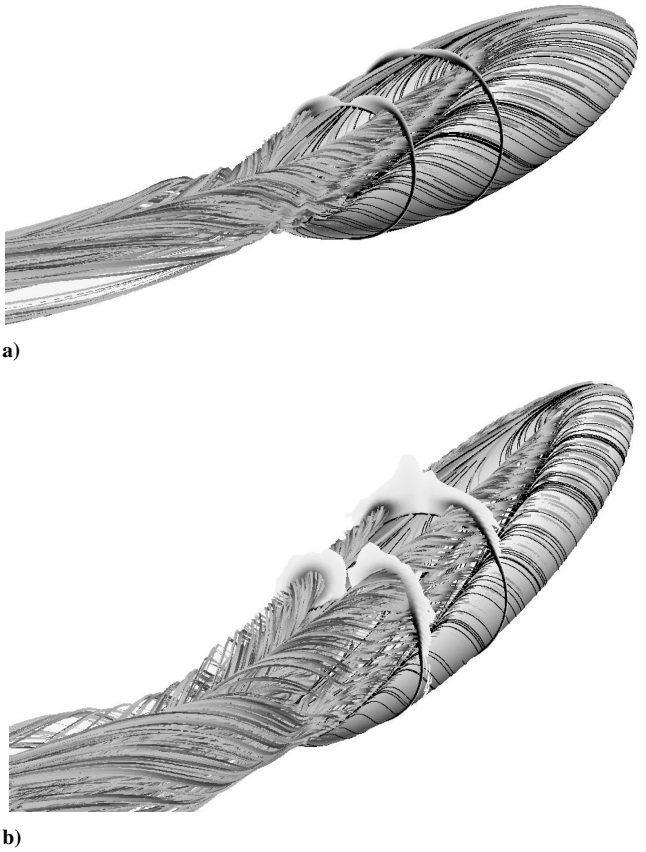

Fig. 9 Perspective view of the crossflow separation and the associated longitudinal vortices on a 6:1 prolate spheroid at a) $\alpha = 10$ deg and b) $\alpha = 20$ deg, respectively.

and surface streamlines. On the windward side, an attached three-dimensional boundary layer is formed, whereas on the leeward side the flow detaches from the hull because of the circumferentially adverse pressure gradient and rolls up into a counter-rotating pair of longitudinal spiraling vortices on the back of the body. Moreover, fluid from the windward side is advected across the spheroid, engulfed into the primary vortices and subsequently ejected into the wake. This primary vortex is sometimes followed by at least one smaller vortex, which separates and reattaches high up on the body. The complex interaction between vortices is strongly dependent on the angle of attack α and the Reynolds number and results in a highly skewed unsteady three-dimensional boundary layer. Boundary-layer detachment is almost always accompanied by undesirable effects such as loss of lift, increases in drag, and amplification of unsteady effects including fluctuations in velocity and pressure. Prediction of three-dimensional separation and the features with which it is associated is difficult, forming one of the main obstacles to more widespread use of CFD in analysis and design.

Here and in Refs. 55 and 56 we consider the flow around a 6:1 prolate spheroid, mounted in a wind tunnel with rectangular cross section.[57–60] The body length is $L = 1.37$ m, and the tunnel cross section is 1.8×1.8 m^2. The freestream velocity is $v_0 = 46$ m/s, creating a body-length Reynolds number of $Re_L = 4.2 \times 10^6$. Detailed measurements have been carried out at angles of attack between $\alpha = 0$ and 30 deg, and here we focus on $\alpha = 10$ and 20 deg. For the simulations to be compared to those of Constantinescu et al.,[61] the computational domain consists of a sphere with radius $R = 2L$. This has the advantage of simplifying gridding, thus producing grids of high quality with modest stretching and skewness. The disadvantage is that the blocking effects are neglected, but these are generally considered small in comparison to neglecting the supporting sting on which the body is mounted and possibly also the effects of the freestream wind-tunnel specific flow.

The grid topology consists of two blocks: an inner O grid that wraps around the body and an outer O grid that fills the region between the inner grid and the outer spherical boundary. Three grids are used in the computations in order to parameterize effects of the grid resolution and of the boundary-layer resolution. Grid A has 0.80×10^6 cells and $y^+ \approx 25$. Grid B is topologically similar to mesh A but with 1.60×10^6 cells and $y^+ \approx 12$. Grid C is also refined to 1.60×10^6 cells, but all added cells are contained in the inner O grid, and the refinement is performed in the normal direction only resulting in a well-resolved boundary layer having $y^+ \approx 4$. At the inlet, $\bar{\boldsymbol{v}} = v_0 \boldsymbol{n}$ and $\partial \bar{p}/\partial \boldsymbol{n} = \boldsymbol{0}$, where $\boldsymbol{n}$ is the outward pointing unit normal, and at the outlet $\bar{p} = p_\infty$ and $\partial(\bar{\boldsymbol{v}} \cdot \boldsymbol{n})/\partial \boldsymbol{n} = \boldsymbol{0}$. On the body, no-slip conditions are utilized. After the initial transients vanishes, the statistical sampling was started, and sufficient time (25,000 time steps) was allowed for each of the runs to develop time-averaged data for the first- and second-order statistical moments of $\bar{p}$ and $\bar{\boldsymbol{v}}$.

Figure 10 shows the static-pressure coefficient $C_P = (\langle p \rangle - p_0)/\frac{1}{2} v_0^2$, where p_0 is a reference pressure 1) in the meridian plane and 2) as a function of φ at $x/L = 0.772$. As seen in Fig. 10a, the agreement between simulations and experiments for $\alpha = 10$ deg is good, especially on the leeward side. Along the windward side in the stern, there is some discrepancy; one contributor could be the presence of the support sting used in the experiments and not included in the LES. Compared to the distribution, at $\alpha = 10$ deg the profiles from the LES at $\alpha = 20$ deg exhibit greater streamwise variation, corresponding to the stronger acceleration of the flow over the body on the windward side and greater decceleration over the leeward side of the body. Considering the influence of the subgrid model and the resolution, we find that all models except the LDKM on grid A predicts C_P virtually identically. In Fig. 10b, C_P is shown as a function of φ at $x/L = 0.772$. For $\alpha = 10$ deg the agreement between LES

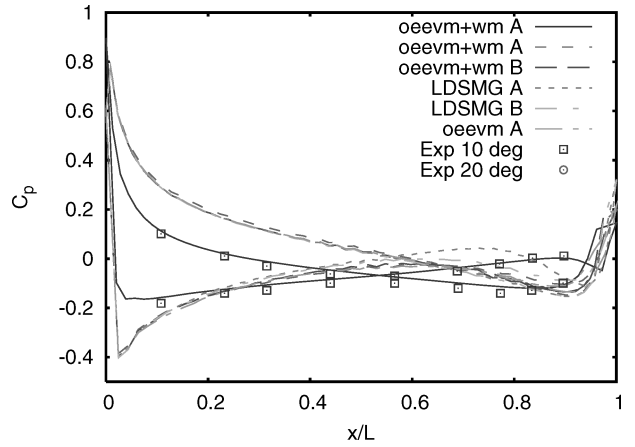

a)

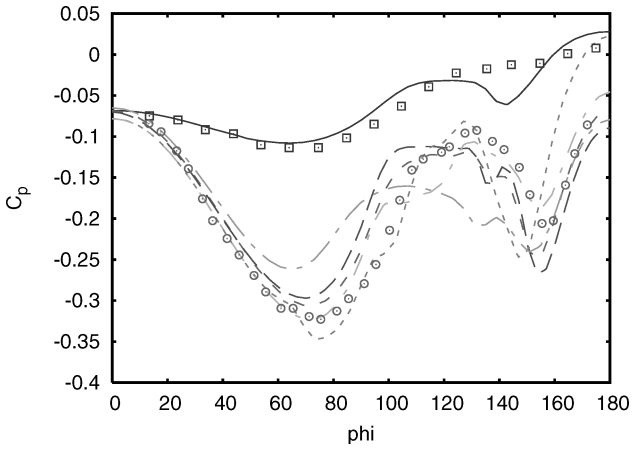

b)

Fig. 10 Comparison of the static-pressure coefficient C_P at a) the meridian plane and b) $x/L = 0.772$.

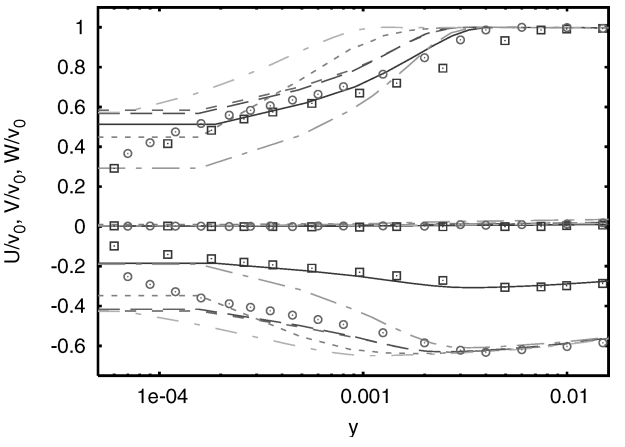

a)

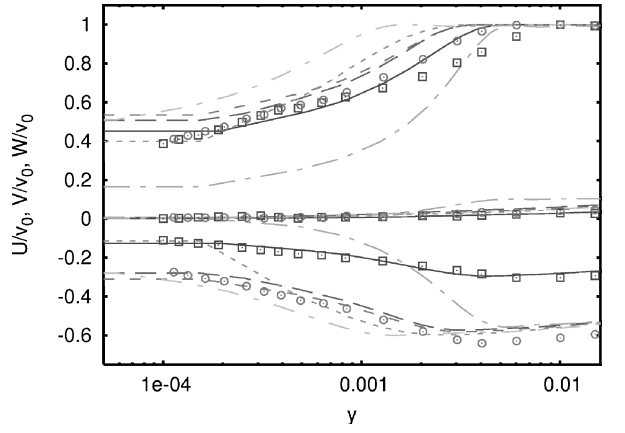

b)

Fig. 11 Comparison of the normalized velocity (U, V, W) in the body surface coordinate system at a) $x/L = 0.600$, $\varphi = 90$ deg and b) $x/L = 0.772$, $\varphi = 90$ deg. For legend, see Fig. 10.

and experimental data is good, with the exception of the sector between $\varphi = 120$ and 150 deg. This corresponds to the region beneath the primary vortex, and from theoretical considerations we expect a low-pressure patch on the hull beneath that vortex. For $\alpha = 20$ deg C_P shows the existence of both a primary and a secondary separation on the body, and the agreement between experimental data and LES is reasonable for runs II, III, and VI, especially on the windward side. The predictions by run IV (the OEEVM on grid A) differs considerably from the other models and the experimental data. Similarly, prediction by run V (the LDKM on grid A) also differs from the experimental data. In addition, the results from run VI (the LDKM on grid C) suggest an early separation at $\alpha \approx 98$ deg. These results show the sensitivity of the predictions to the models and the grid and suggest that the LDKM requires finer resolution than the OEEVM + WM.

Figure 11 shows the normalized time-averaged boundary-layer velocity profiles at two rakes at $x/L = 0.600$, $\varphi = 90$ deg, and at $x/L = 0.772$, $\varphi = 90$ deg, respectively, for $\alpha = 10$ and 20 deg. The velocity components are presented in the body-surface coordinate system.[60] Here, U is tangent to the body and point toward the tail of the model, V is normal to the body (positive outwards), and W is tangent to the body and forms a right-handed coordinate system. LES qualitatively captures the influence of the angle of attack that is evident from the increase in V in the outer part of the boundary layer. This increase in V is caused by fluid being extracted from the boundary layer into the primary vortices on the back of the body. For the normal (or V) component good agreement with experimental data is obtained for the OEEVM + WM irrespectively of grid resolution and for both angles of attack. For $\alpha = 20$ deg the OEEVM model produces poor V profiles, which is believed to be caused by the insufficient generality of the van Driest damping function in combination with the modest resolution for flows with moderate-to-strong pressure gradients. For the tangential (or W) component we find that all LES models reproduce the experimental data fairly well. For the axial (or U) component we find reasonable agreement between predictions using the OEEVM + WM on all grids and the experimental data for both angles of attack, suggesting that this model 1) can capture the flow effects caused by the angle of attack and 2) is insensitive to the resolution in the near-wall region. The OEEVM (with van Driest damping) on grid A gives poor agreement with the data and with the other model predictions. The LDKM produces too thin boundary layers, and the resulting vortices are therefore located too close to the body. In general, the agreement between the LES and the experimental data is reasonable considering the complexity of the flow, and we also find reasonable agreement with the DES results in Ref. 61.

Figure 12 shows secondary streamlines superimposed on contours of U. These comparisons reveal the difference in grid sensitivity between LDKM and OEEVM + WM. The OEEVM + WM predictions appear virtually unaffected by the resolution, whereas the LDKM results are dependent on the grid resolution. This is not surprising considering the details of the models and how the subgrid eddy viscosity is calculated. Comparing with measured secondary streamlines and velocity contours (not shown), we notice that both models capture the key flow features, with the OEEVM + WM being in better quantitative agreement with the measurement data, with larger and more pronounced primary vortices. Both the location and strengths of the primary vortices are changed when the grid is refined (as in run VI). Furthermore, the low-speed finger stretching toward the vortex core is not as significant for the LDKM as it is for the OEEVM + WM. This is closely related to the difference in boundary-layer thickness and shape presented and discussed in

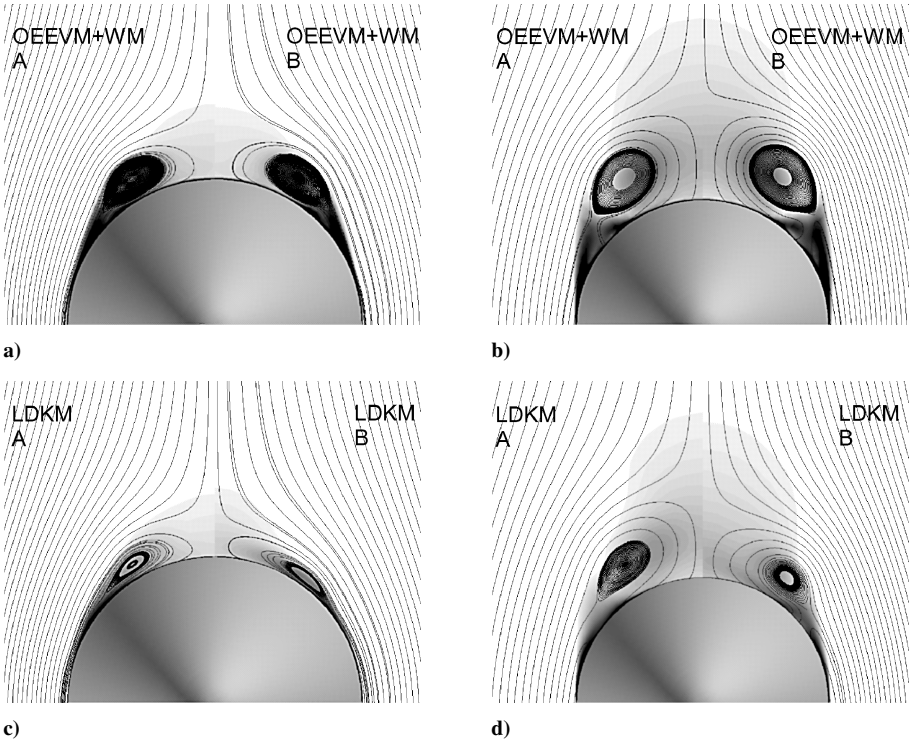

Fig. 12 Secondary streamlines superimposed on U at $x/L = 0.600$ (a and c) and $x/L = 0.772$ (b and d) for cases II (left part of a and b), III (right part of a and b), V (left part of c and d), and VI (right part of c and d).

Table 1 Summary of selected run configurations

Run	α	Grid	LES subgrid model	$\tilde{n}$, φ at $x/L = 0.77$[a,b]
EXP	10	——	——	1.2 cm, 145 deg
I	10	A	OEEVM + WM	1.3 cm, 145 deg
EXP	20	——	——	3.0 cm, 155 deg
II	20	A	OEEVM + WM	3.2 cm, 152 deg
III	20	B	OEEVM + WM	3.2 cm, 152 deg
IV	20	A	OEEVM (van Driest)	3.2 cm, 152 deg
V	20	A	LDKM	2.9 cm, 150 deg
VI	20	C	LDKM	2.5 cm, 146 deg

[a] $\tilde{n}$ is the distance from the prolate spheroid hull to the vortex core.
[b] φ is the associated circumferential angle.

Fig. 11. However, the secondary vortex is better predicted with the LDKM. Concerning the flow features, the most significant difference is that the finger of low-velocity fluid that stretches from the wall out toward the core of the vortex at $x/L = 0.772$ is slightly stronger on grid B. In Table 1 we show the locations (distance $\tilde{n}$ and angle φ) of the primary vortices. These results corroborate that the best overall agreement is obtained with the OEEVM+WM, which for this case appears virtually independent of the grid topology and resolution.

IX. Summary

When large-eddy simulation (LES) is used to study building-block flows for which the method originally was invented, it produces good results, and the dependency of the results on the subgrid model is only weak. For free flows reasonable agreement is generally obtained also for high-Reynolds-number flows. However, for high-Reynolds-number wall-bounded flows, LES becomes more involved because the dynamically important scales become smaller and smaller as the wall is approached. As Reynolds number increases, we cannot afford resolving all scales even if local grid refinement or adaptive meshes are used. This puts additional demands on the subgrid model, which in this case can be combined with a separate wall model, as frequently done in Reynolds-averaged Navier–Stokes (RANS). Here, we have investigated a few conventional LES models, alternative LES models, and two emerging new LES approaches.

As demostrated by the LES calculations presented here, the most significant challenges and perhaps the main pacing item for LES is improved methodologies for modeling near-wall turbulence at high Reynolds number. The large-scale structure of turbulent flows near walls is affected by mean shear, kinematic blocking, fluctuating pressure reflections, and by moving internal shear layers produced by the large-scale structures. Elongated streamwise vortices are formed. These structures mix high-momentum fluid in the outer part of the boundary layer with low-momentum fluid from the near-wall region. These processes are believed to be responsible for the generation of turbulent shear stresses and the subsequent modification of the mean flowfield. Because we cannot afford to resolve the details of the near-wall flow, we are forced to model the small-scale flow features that are important in the near-wall region. In the channel flow simulations these features are present on some level—either resolved or partially resolved—depending on Reynolds number and the grid. In the more complicated cases these processes are partially resolved, at the best, and the subgrid model is of more importance to the outcome of the LES calculation.

From a mathematical perspective, the deficiency of the eddy-viscosity approach [Eq. (4)] is apparent: formally it does not match the leading-order terms of Eq. (3), whereas similarity and mixed models do share some formal similarities with the Taylor-series expansion model in Eq. (3). A priori analysis of the correlation coefficients between the exact and modeled subgrid-stress tensor supports this, showing low values (about 0.2) for the eddy-viscosity models and higher values (about 0.8) for scale-similarity and mixed model [Eq. (5)]. However, a posteriori LES using eddy-viscosity models generally gives reasonable results, in particular if the model coefficients are evaluated dynamically and if the grid is reasonably fine. The explanation for this appears to be that the eddy-viscosity responds to the accumulation of energy in the small scales by adjusting the dissipation before it contaminates the resolved scales, although $\boldsymbol{B}$ is not generally alined with $\bar{\boldsymbol{D}}$. Structural models [e.g., scale-similarity model, differential-stress-equation model (DSM), and approximate-deconvolution mode (ADM)] are therefore better suited for complex anisotropic flows but are not always numerically stable. Monotone-integrated large-eddy simulation (MILES), on the other hand, provides an interesting alternative, being related to both structural and functional models, but is associated with

the advantage/drawback of its strong coupling with the numerical schemes used. Wall models also provide an attractive alternative, but appear to be sensitive to the flow condition and are not allowed to deviate too much from the flat-plate boundary layer for which they are developed.

If we in the future want to use LES for more complicated engineering flow problems at high Reynolds numbers, the subgrid models have to evolve. Traditional models are not sufficiently accurate or detailed, and more advanced models are required. These models must cater for the highly anisotropic flow in the near-wall region and can thus be constructed using, for example, differential-stress models, subgrid-simulation models, homogenization techniques, or other models carrying information about the structures of the small-scale flow, either directly or in some parameterized form. At present, the ADM, DSM, MILES, and two-level-simulation (TLS) models probably holds most promise for the future, although each model has its own disadvantages. For example, the TLS and DSM models are computationally more expensive, and the MILES approach is closely tied to the numerics.

Acknowledgments

This work is partly supported by the Swedish Defence Material Administration under Grant Marine LES and by the Office of Naval Research. High-performing-computing (HPC) resources are provided by FOI, Sweden, and by the U.S. Department of Defence HPC centers at Maui, Hawaii, and NAVOCEANO, Alabama. Some of the presented computations were performed with an earlier research version of the FOAM™ code; for further details, see http://www.nabla.com.uk.

References

[1]Speziale, C. G., "Modeling of Turbulent Transport Equations," *Simulation and Modeling of Turbulent Flows*, edited by T. B. Gatski, M. Y. Hussaini, and J. L. Lumley, Oxford Univ. Press, New York, 1996, p. 185.

[2]Wilcox, D. C., *Turbulence Modeling for CFD*, DCW Industries, 1998.

[3]Pope, S. B., *Turbulent Flows*, Cambridge Univ. Press, Cambridge, England, U.K., 2000.

[4]Ferziger, J. H., and Leslie, D. C., "Large Eddy Simulation—A Predictive Approach to Turbulent Flow Computation," AIAA Paper 79-1441, 1979.

[5]Sagaut, P., *Large Eddy Simulation for Incompressible Flows*, Springer-Verlag, Heidelberg, Germany, 2001.

[6]Fureby, C., "Towards Large Eddy Simulation of Complex Flows," *Direct and Large Eddy Simulation IV*, edited by R. Friedrich and W. Rodi, Kluwer, Amsterdam, 2001, pp. 165–184.

[7]Lesieur, M., and Metais, O., "New Trends in Large Eddy Simulations of Turbulence," *Annual Review of Fluid Mechanics*, Vol. 28, 1996, p. 45.

[8]Boris, J. P., Grinstein, F. F., Oran, E. S., and Kolbe, R. L., "New Insights into Large Eddy Simulation," *Fluid Dynamic Research*, Vol. 10, 1992, pp. 199–229.

[9]Grinstein, F. F., and Karniadakis, G. E., "Special Section on Alternative LES and Hybrid RANS/LES for Turbulent Flows," *Journal of Fluids Engineering*, Vol. 124, 2002, pp. 821–832.

[10]Bagget, J. S., Jiménez, J., and Kravchenko, A. G., "Resolution Requirements in Large Eddy Simulations of Shear Flows," *CTR Annual Research Briefs*, 1997, pp. 51–66.

[11]Ghosal, S., and Moin, P., "The Basic Equations for the Large Eddy Simulation of Turbulent Flows in Complex Geometry," *Journal of Computationl Physics*, Vol. 118, 1995, pp. 24–37.

[12]Fureby, C., and Tabor, G., "Mathematical and Physical Constraints on Large Eddy Simulations," *Journal of Theoretical Fluid Dynamics*, Vol. 9, 1997, pp. 85–102.

[13]Vreman, B., Geurts, B., and Kuerten, H., "Realizability Conditions for the Turbulent Stress Tensor in Large Eddy Simulation," *Journal of Fluid Mechanics*, Vol. 278, 1994, pp. 351–362.

[14]Speziale, C. G., "Galilean Invariance of Sub Grid Scale Stress Models in the Large Eddy Simulation of Turbulence," *Journal of Fluid Mechanics*, Vol. 156, 1985, pp. 55–62.

[15]Carati, D., Winckelmans, G. S., and Jeanmart, H., "Exact Expansions for Filtered Scales Modeling with a Wide Class of LES Filters," *Direct and Large Eddy Simulation III*, edited by P. Voke, N. Sandham, and L. Kleiser, 1999, pp. 213–224.

[16]Geurts, B. J., "Balancing Errors in LES," *Direct and Large Eddy Simulation IV*, edited by R. Friedrich and W. Rodi, Kluwer, Amsterdam, 2001, pp. 13–31.

[17]Schumann, U., "Subgrid Scale Model for Finite Difference Simulation of Turbulent Flows in Plane Channels and Annuli," *Journal of Computational Physics*, Vol. 18, 1975, pp. 376–404.

[18]Smagorinsky, J., "General Circulation Experiments with the Primitive Equations. I. The Basic Experiment," *Monthly Weather Review*, Vol. 91, 1963, pp. 99–165.

[19]Germano, M., Piomelli, U., Moin, P., and Cabot, W. H., "A Dynamic Sub Grid Scale Eddy Viscosity Model," *Physics of Fluids A,* Vol. 3, 1994, pp. 1760–1765.

[20]Ghosal, S., Lund, T. S., Moin, P., and Akselvoll, K., "A Dynamic Localization Model for Large Eddy Simulation of Turbulent Flows," *Journal of Fluid Mechanics*, Vol. 286, 1995, pp. 229–255.

[21]Meneveau, C., Lund, T. S., and Cabot, W. H., "A Lagrangian Dynamic Subgrid-Scale Model of Turbulence," *Journal of Fluid Mechanics*, Vol. 319, 1996, pp. 353–385.

[22]Kim, W.-W., and Menon, S., "A New Dynamic One Equation Sub Grid Scale Model for Large Eddy Simulations," AIAA Paper 95-0356, Jan. 1995.

[23]Kim, W.-W., and Menon, S., "A New Incompressible Solver for Large-Eddy Simulations," *International Journal for Numerical Fluid Mechanics*, Vol. 31, 1999, p. 983.

[24]Bardina, J., Ferziger, J. H., and Reynolds, W. C., "Improved Subgrid Scale Models for Large Eddy Simulations," AIAA Paper 80-1357, Jan. 1980.

[25]Deardorff, J. W., "The Use of Subgrid Transport Equations in a Three-Dimensional Model of Atmospherical Turbulence," *Journal of Fluids Engineering Transactions*, Vol. 95, 1973, pp. 429–438.

[26]Fureby, C., Tabor, G., Weller, H., and Gosman, D., "On Differential Sub Grid Scale Stress Models in Large Eddy Simulations," *Physics of Fluids*, Vol. 9, 1997, pp. 3578–3580.

[27]Lund, T. S., and Novikov, E. A., "Parameterization of Subgrid-Scale Stress by the Velocity Gradient Tensor," *CTR Annual Research Briefs*, 1994, pp. 27–43.

[28]Wang, M., "Progress in Large Eddy Simulation of Trailing Edge Turbulence and Aeroacoustics," *CTR Annual Research Briefs*, 1997, pp. 37–49.

[29]Wang, M., and Moin, P., "Wall Modeling in LES of Trailing Edge Flow," *Turbulence and Shear Flow Phenomena*, Vol. 2, edited by E. Lindborg et al., 2001, p. 165.

[30]Spalart, P. R., and Allmaras, S. R., "A One-Equation Turbulence Model for Aerodynamic Flows," AIAA Paper 92-0439, 1992.

[31]Spalart, P. R., Jou, W.-H., Strelets, M., and Allmaras, S. R., "Comments on the Feasibility of LES for Wings, and on a Hybrid RANS/LES Approach," *Advances in DNS/LES*, Greyden Press, Columbus, OH, 1997.

[32]Nikitin, N. V., Nicoud, F., Wasistho, B., Squires, K. D., and Spalart, P. R., "An Approach to Wall Modeling in Large Eddy Simulations," *Physics of Fluids*, Vol. 12, 2000, pp. 1629–1631.

[33]Boris, J. P., and Book, D. L., "Flux Corrected Transport I, SHASTA, a Fluid Transport Algorithm that Works," *Journal of Computational Physics*, Vol. 11, 1973, pp. 38–69.

[34]Fureby, C., and Grinstein, F. F., "Large Eddy Simulation of High Reynolds Number Free and Wall Bounded Flows," *Journal of Computational Physics*, Vol. 181, 2002, pp. 68–97.

[35]Garnier, E., Mossi, M., Sagaut, P., Comte, P., and Deville, M., "On the Use of Shock-Capturing Schemes for Large Eddy Simulation," *Journal of Computational Physics*, Vol. 153, 2000, pp. 273–311.

[36]Okong'o, N., Knight, D. D., and Zhou, G., "Large Eddy Simulations Using an Unstructured Grid Compressible Navier–Stokes Algorithm," *International Journal of Computational Fluid Dynamics*, Vol. 13, 2000, pp. 303–326.

[37]Margolin, L. G., Smolarkiewicz, P. K., and Sorbjan, Z., "Large-Eddy Simulation of Convective Boundary Layers Using Non-Oscillatory Differencing," *Physica D*, Vol. 133, 1999, pp. 390–397.

[38]Karamanos, G.-S., and Karniadakis, G. E., "A Spectral Vanishing Viscosity Method for Large-Eddy Simulations," *Journal of Computational Physics*, Vol. 163, 2000, pp. 22–50.

[39]Grinstein, F. F., and Fureby, C., "Recent Progress on MILES for High Re Flows," *Journal of Fluids Engineering*, Vol. 124, 2002, pp. 848–861.

[40]Adams, N. A., and Stolz, S., "Deconvolution Methods for Subgrid-Scale Approximation in LES," *Modern Simulation Strategies for Turbulent Flows*, edited by B. J. Geurts, Edwards, Philadelphia, 2001, p. 21.

[41]Stolz, S., Adams, N. A., and Kleiser, L., "An Approximate Deconvolution Model for Large-Eddy Simulation of Incompressible Flows," *Physics of Fluids*, Vol. 11, 1999, pp. 1699–1701.

[42]Van Cittert, P. H., *Z. Physik*, Vol. 69, 1931, p. 298.

[43]Tikhonov, A. N., and Arsenin, V. Y., *Solutions of Ill-Posed Problems*, Wiley, New York, 1977.

[44]Kemenov, K., and Menon, S., "TLS: A New Two Level Simulation Methodology for High-Reynolds LES," AIAA Paper 2002-0287, Jan. 2002.

[45]Kemenov, K., and Menon, S., "A Two-Level Simulation of High-Reynolds Number Non-Homogeneous Turbulent Flows," AIAA Paper 2003-0084, Jan. 2003.

[46]Kerstein, A., "One-Dimensional Turbulence: Model Formulation and Application to Homogeneous Turbulence, Shear Flows and Buyoant Stratified Flows," *Journal of Fluid Mechanics*, Vol. 392, 1999, pp. 277–334.

[47]Persson, L., Fureby, C., and Svanstedt, N., "On Homogenisation Based Methods for Large Eddy Simulation," *Journal of Fluids Engineering*, Vol. 124, 2002, pp. 892–903.

[48]Bensoussan, A., Lions, J. L., and Papanicolaou, G., *Asymptotic Analysis for Periodic Structures*, North-Holland, 1978.

[49]Weller, H. G., Tabor, G., Jasak, H., and Fureby, C., "A Tensorial Approach to CFD Using Object Oriented Techniques," *Computers in Physics*, Vol. 12, 1997, pp. 620–631, URL:http://www.nabla.com.uk.

[50]Moser, R. D., Kim, J., and Mansour, N. N., "Direct Numerical Simulation of Turbulent Channel Flow up to $Re_\tau = 590$," *Physics of Fluids*, Vol. 11, 1999, pp. 943–945.

[51]Wei, T., and Willmarth, W. W., "Reynolds Number Effects on the Structure of a Turbulent Channel Flow," *Journal of Fluid Mechanics*, Vol. 204, 1989, pp. 57–95.

[52]Simpson, R., Long, C., and Byun, G., "Study of Vortical Separation from an Axisymmetric Hill," *International Journal of Heat and Fluid Flow* (to be published).

[53]Simpson, R., "Structure of Rough-Wall Three-Dimensional Turbulent Boundary Layers and Vortical Separations," *Turbulence and Wakes Program Review*, Office of Naval Research, 2001.

[54]Patel, N., Stone, C., and Menon, S., "Large Eddy Simulation of Turbulent Flow Over an Axisymmetric Hill," AIAA Paper 03-0967, 2003.

[55]Wikström, N., Svennberg, U., Alin, N., and Fureby, C., "Large Eddy Simulation of the Flow past an Inclined Prolate Spheroid," TSFP 3, Sendai, Japan, June 2003.

[56]Wikström, N., Svennberg, U., Alin, N., and Fureby, C., "LES of the Flow Past an Inclined Prolate Spheroid," *Journal of Turbulence* (submitted for publication).

[57]Barber, K. M., and Simpson, R. L., "Mean Velocity and Turbulence Measurements of Flow Around a 6:1 Prolate Spheroid," AIAA Paper 91-0255, Jan. 1991.

[58]Chesnakas, C. J., and Simpson, R. L., "Measurements of Turbulence Structure in the Vicinity of a 3D Separation," *Journal of Fluids Engineering*, Vol. 118, 1996, pp. 268–275.

[59]Wetzel, T. G., Simpson, R. L., and Chesnakas, C. J., "Measurement of Three-Dimensional Crossflow Separation," *AIAA Journal*, Vol. 36, 1998, pp. 557–564.

[60]Simpson, R. L., "Steady Flow Over a 6:1 Prolate Spheroid," *Journal of Fluids Engineering*. [on line databank] URL:http://www.aoe.vt.edu/aoe/prolatespheroid [cited 2000].

[61]Constantinescu, G. S., Pasinato, H., Wang, Y.-Q., Forsythe, J. R., and Squires, K. D., "Numerical Investigation of Flow past a Prolate Spheroid," AIAA Paper 02-0588, Jan. 2002.

F. Grinstein
Guest Editor

Orbital Mechanics, Third Edition

Vladimir A. Chobotov • The Aerospace Corporation

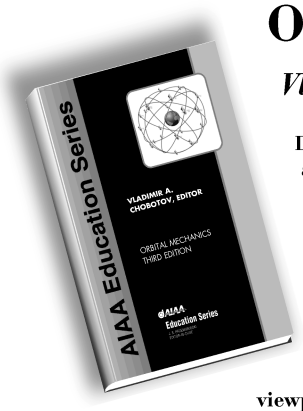

Designed to be used as a graduate student textbook and a ready reference for the busy professional, this third edition of *Orbital Mechanics* is structured to allow you to look up the things you need to know. This edition includes more recent developments in space exploration (e.g. Galileo, Cassini, Mars Odyssey missions). Also, the chapter on space debris was rewritten to reflect new developments in that area.

The well-organized chapters cover every basic aspect of orbital mechanics, from celestial relationships to the problems of space debris. The book is clearly written in language familiar to aerospace professionals and graduate students, with all of the equations, diagrams, and graphs you would like to have close at hand.

An updated software package on CD-ROM includes: HW Solutions, which presents a range of viewpoints and guidelines for solving selected problems in the text; Orbital Calculator, which provides an interactive environment for the generation of Keplerian orbits, orbital transfer maneuvers, and animation of ellipses, hyperbolas, and interplanetary orbits; and Orbital Mechanics Solutions.

Contents

- Basic Concepts
- Celestial Relationships
- Keplerian Orbits
- Position and Velocity as a Function of Time
- Orbital Maneuvers
- Complications to Impulsive Maneuvers
- Relative Motion in Orbit
- Introduction to Orbit Perturbations
- Orbit Perturbations: Mathematical Foundations
- Applications of Orbit Perturbations
- Orbital Systems
- Lunar and Interplanetary Trajectories
- Space Debris
- Optimal Low-Thrust Orbit Transfers
- Orbital Coverage

AIAA

American Institute of Aeronautics and Astronautics
Publications Customer Service, P.O. Box 960, Herndon, VA 20172-0960
Fax: 703/661-1501 • Phone: 800/682-2422 • E-Mail: warehouse@aiaa.org
Order 24 hours a day at www.aiaa.org

2002, 460 pages, Hardback, with Software
ISBN: 1-56347-537-5
List Price: $100.95 • AIAA Member Price: $69.95

02-0546